Layer-by-layer assembly of sol–gel oxide "glued" montmorillonite-zirconia multilayers

Hao Chen,[a] Guoping Zhang,[b] Zhongxin Wei,[b] Kevin M. Cooke†[c] and Jian Luo*[ad]

Received 27th January 2010, Accepted 13th March 2010
First published as an Advance Article on the web 30th April 2010
DOI: 10.1039/c0jm00177e

This paper reports the layer-by-layer synthesis and growth kinetics of a new class of nanostructured multilayers consisting of montmorillonite (MMT) nanoclays "glued" by sol–gel oxides, such as zirconia (ZrO_2) and tin oxide (SnO_2), $\{MMT_x\text{-(sol–gel oxide)}\}_n$. The multilayers possess an ordered layer structure with tunable nanoscale periods of thickness. Systematic investigation of growth kinetics revealed unique underlying film growth mechanisms. The growth of the MMT and sol–gel ZrO_2 layers is strongly coupled. For fresh aqueous ZrO_2 precursors, the growth rates of sol–gel ZrO_2 layers on MMT surfaces as functions of time and precursor concentration do not follow the standard mass transfer or interfacial reaction controlled kinetic models. Furthermore, the growth of the sol–gel oxide layers on MMT surfaces is self-limited to a maximum thickness of ~50–60 nm. These observations suggest a surface-mediated growth of sol–gel oxide layers on MMT surfaces, and such growth is likely influenced or controlled by electrostatic interactions. For the aged precursors, the growth mechanism differs; the growth of sol–gel oxide layers is controlled by hydrodynamics and follows the Landau–Levich model. These new findings on detailed growth kinetics, which have been difficult to observe and quantify *via* the synthesis of more prevailing polyelectrolyte-based multilayers, significantly advance the general understanding of the layer-by-layer electrostatic assembly. Overall, layer-by-layer assembly of multilayers using sol–gel oxides, instead of polyelectrolytes, as both adhesive and functional components in the structure, is a new concept of nanoscale fabrication, which can lead to the development of a broad range of inorganic nanostructured films. The mechanical properties and potential applications of this new class of multilayers are briefly discussed.

1. Introduction

The layer-by-layer (LbL) electrostatic assembly technique fabricates nanostructured multilayers *via* sequential deposition of oppositely charged species onto a surface through electrostatic attraction.[1–9] In the 1990s, Decher *et al.* developed a LbL method to make polyelectrolyte multilayers.[10,11] Following this work, a wide range of organic and hybrid organic–inorganic films with a broad spectrum of mechanical, electrical, and biological functionalities[1–9] were developed, using building units such as polyelectrolytes, nanoparticles, dyes,[12] proteins,[13] and enzymes. These LbL methods have a number of advantages, including high versatility for film composition, ease of preparation, low cost, precise control of layer thickness,[14] and self-healing.[15,16] Several recent reviews[1–9] have summarized the broad applications of these LbL assembled multilayers.

Recently, a class of polyelectrolyte–nanoclay multilayers has attracted great attention.[1,13,15,17–23] Many of such multilayers utilize exfoliated montmorillonite (MMT), in which isomorphous substitution results in net negatively charged surfaces,[24] enabling electrostatic assembly. Furthermore, the high aspect ratio of exfoliated MMT of ~1 nm in thickness and 100–1000 nm in lateral dimension[25] provides a planar surface for the deposition and growth of oppositely charged units. In particular, Kotov's group synthesized "artificial nacres",[21] and these polymer–nanoclay multilayers exhibit strength and stiffness close to those of steels.[23] Their studies demonstrated that nanocomposites can possess the promised superior mechanical (and other) properties with controlled, manipulated nanoscale fabrication.[26–32] Based on the literature, nanoclay-based multilayers have a wide range of potential applications, such as gas membranes,[17] diffusion barriers,[33] mechanically protective coatings,[21,23] sensor materials,[34,35] anti-corrosion coatings,[36] and microcantilevers.[33]

To date, a majority of the electrostatically assembled films consist of either all or partial polyelectrolyte layers that serve as the "electrostatic glue" for structural integrity. On the other hand, all-inorganic multilayers are attractive for applications in high-temperature environments, and they usually exhibit better rigidity and chemical stability than polymer-bearing multilayers. Only a few types of multilayers with primarily inorganic building units, typically nanoparticles, have been synthesized. In 1966, Iler *et al.* at DuPont developed probably the first electrostatically

[a]*School of Materials Science and Engineering, Clemson University, Clemson, South Carolina, 29634, USA. E-mail: jluo@alum.mit.edu*
[b]*Department of Civil and Environmental Engineering, Louisiana State University, Baton Rouge, Louisiana, 70803, USA*
[c]*The Calhoun Honors College EUREKA! Program, Clemson University, Clemson, South Carolina, 29634, USA*
[d]*Center for Optical Materials Science and Engineering Technologies, Clemson University, Anderson, South Carolina, 29625, USA*
† Present affiliation: Department of Physics and Astronomy, Clemson University, Clemson, South Carolina 29634, USA.

assembled multilayers using SiO_2 and boehmite fibrils,[37] although this work did not receive much attention at that time. In 2006, Lee *et al.* at MIT re-examined the possibility of making "all-nanoparticle" multilayer films through LbL electrostatic assembly using TiO_2 and SiO_2 nanoparticles.[38,39] In 2008, they further made multilayers of oppositely charged SiO_2 nanoparticles with alternate surface charges changed by surface modification.[40] In the same year, the synthesis of another multilayer of MnO_2 nanosheets and layered double hydroxides was reported.[41] In 2009, another MIT group synthesized all carbon nanotube multilayers[42] and carbon nanotube/Au nanoparticle thin films,[43] both involving surface modification to alter surface charges. Other examples include multilayers of coated Au/Ag nanoparticles[44,45] and modified CdS/TiO_2 nanoparticles, and polyelectrolyte-glued multilayers of $\{TiO_2\text{-}Ti_{1-\delta}O_2\}_n$,[46] $\{Ag\text{-}Ti_{1-\delta}O_2\}_n$,[47] and $\{clay\text{-}Fe_3O_4\}_n$.[48,49] All of these primarily inorganic multilayers were based on inorganic nanoparticles, including nanotubes and nanosheets, and many of them employed surface modifications using organic species to enable electrostatic assembly.

In a preliminary report,[50] we proposed a method to synthesize a new type of all-inorganic $\{MMT_x\text{-(sol–gel } ZrO_2)\}_n$ multilayers by combining the LbL electrostatic assembly technique with a surface sol–gel method.[51,52] In this paper, we report an optimized method to synthesize such multilayers with much improved layered, periodic structures. Results demonstrate the capability to finely tune the nanoscale periodic layer thickness.

Most importantly, this paper reports some newly observed film growth kinetics controlling the sol–gel ZrO_2 layer deposition on the MMT surfaces, which elucidates the role of electrostatic attraction in film growth. Specific findings include: 1) the growth rates of the sol–gel ZrO_2 layers are significantly enhanced on the MMT surface; 2) the intermediate-stage growth rates of the sol–gel ZrO_2 layers on the MMT surface are greater than those estimated by either mass transfer or interfacial reaction controlled kinetic models; and 3) the growth of sol–gel ZrO_2 layers on the MMT surface is self-limited to a maximum thickness. These phenomena are attributed to the surface controlled sol–gel growth that is likely influenced or controlled by electrostatic attractions.

Although the mechanisms of the electrostatic assembly are important and have been extensively investigated,[1–9,53–57] quantitative studies have been generally difficult. This is largely caused by the use of polyelectrolytes in the synthesis of those LbL films, which results in so-called "fuzzy multilayers".[53] Thus, this study of the film growth kinetics, *via* synthesizing the $\{MMT_x\text{-(sol–gel } ZrO_2)\}_n$ multilayers, provides a different perspective to the quantitative understanding of the film growth kinetics. The findings improve our understanding of the LbL assembly process in its general sense.

Finally, this study has paved the way towards the further development of generic LbL methods to synthesize new, all-inorganic $\{nanosheet_x\text{-(sol–gel oxide)}\}_n$ and $\{nanoparticle\text{-(sol–gel oxide)}\}_n$ multilayers with potential applications such as high-temperature gas membranes and sensors, among others. We have demonstrated that this newly developed technique can be extended to other sol–gel metal oxides by successfully making a $\{MMT_x\text{-(sol–gel } SnO_2)\}_{30}$. Specifically, the LbL assembly of nanostructured multilayers using sol–gel oxides, instead of polyelectrolytes, as "glues" in the structure, represents an innovative concept of nanoscale fabrication.

2. Experimental

Surface polished p-type single-crystal silicon wafers (MEMC Electronic Materials, Inc., St. Peters, MO) were used as substrates for LbL deposition. The wafer surface has a layer of thermally oxidized SiO_2 of 100 nm in thickness, which serves as an inert diffusion barrier. A sodium montmorillonite (MMT) clay, Cloisite® Na^+, with a cation exchange capacity of 92 meq per 100 g was purchased from Southern Clay Products, Inc. (Gonzales, TX). A zirconium(IV) acetate hydroxide ($((CH_3COO)_aZr(OH)_b$, $a + b = 4$; 40 wt.% zirconium or $a \approx 1.5$) powder was purchased from Sigma-Aldrich, Inc. (St. Louis, MO). The MMT and zirconium acetate hydroxide were the two major constituents used for multilayer synthesis.

Small pieces of silicon wafers (with an approximate size of 1×2 cm^2) were ultrasonically cleaned in 0.1 M NaOH solutions for 20 min, immersed into piranha solutions (3 vol. of 95–98 wt.% H_2SO_4 : 1 vol. of 30 wt.% H_2O_2) for 20 min, then rinsed with deionized water four times and dried in air. Different from our preliminary work,[50] this study adopted an improved method to prepare nominally 0.5 wt.% dispersed clay suspensions by following the recipe of Podsiadlo *et al.*,[23] in which the sodium MMT suspensions were first vigorously stirred for a week and then settled for 24 h (to allow the coarser particles and impurities to settle) before supernatants were collected for subsequent LbL assembly. This adoption for better exfoliated clay suspensions, along with the optimization of the sol–gel recipes and dipping processes, significantly improved the ordering of the layered structure and the integrity of the resultant $\{MMT_x\text{-(sol–gel } ZrO_2)\}_n$ multilayers. Aqueous sol–gel ZrO_2 precursors were prepared by dissolving zirconium acetate hydroxide into deionized water along with 20 min ultrasonication. Then, the sol–gel ZrO_2 precursor (which is interchangeably referred as "zirconium acetate hydroxide solution", although the precursor is likely an aqueous polymeric "sol") and the exfoliated MMT suspension were used for subsequent LbL electrostatic assembly.

A computer-controlled programmable dip coater (Nima Technology Ltd., Coventry, UK) was used to perform the LbL deposition. After an extensive parametric study, we selected an optimized synthesis protocol, which consists of four dipping steps: a pre-cleaned substrate was dipped into a sol–gel oxide precursor solution, an MMT suspension, and then deionized water twice. These four steps make up one deposition cycle. Most specimens were prepared with 30 deposition cycles, resulting in $\{MMT_x\text{-(sol–gel } ZrO_2)\}_{30}$ multilayers. The substrate dipping and withdrawing speeds were kept at a fixed value of 20 mm per minute. The substrate was held in static air between two adjacent dips in the precursor solution and MMT suspension. This holding time was usually 45 s in air. Holding was also used in the precursor solution, MMT suspension, and deionized water. Holding durations of 45 s and 1 min in the MMT suspension and water, respectively, were adopted, but the holding time in the precursor solution was varied from 0 to 10 min. Additionally, the precursor concentration varied from 0.03 to 0.4 M. For brevity, specimens were usually referred to according to the precursor concentration and holding time in zirconium acetate hydroxide

solution; other dipping parameters were usually kept unchanged (unless otherwise specified) in this study. After completing the desired deposition cycles, all specimens were air dried and then characterized using the methods described below. Selected specimens were further annealed isothermally to preset temperatures (ranging from 200 to 600 °C) for 2 h in air with a box furnace, using constant heating and cooling rates of 5 °C per minute.

The effect of precursor solution aging on the growth of sol–gel ZrO_2 layers was also examined. Fresh zirconium acetate hydroxide solutions with a concentration of 0.15 M were selected for aging, with durations varying from 0 and 21 h at 60 °C. Aged precursor solutions were then used for LbL assembly of multilayers by following the procedures described above.

Freestanding multilayers were prepared by adopting the procedure used by Mamedov and Kotov for making polyelectrolyte–nanoclay multilayers.[48] It involves a one-time extra step where the pre-cleaned substrate was first dipped into a 7.5 wt.% cellulose acetate solution, before the subsequent dips in other solutions and suspensions. To obtain freestanding films, the air-dried specimens were immersed in acetone to dissolve the cellulose acetate layer, allowing the separation between the desired multilayer and the substrate. As such, freestanding multilayers were conveniently obtained.

As-deposited (*i.e.*, air-dried) and annealed multilayers were characterized by a field-emission scanning electron microscope (FE-SEM, Hitachi S4800). To examine the layered structure and measure the film thickness, cross-sectional surfaces of the specimens were obtained by cleaving the silicon single crystal substrates along the [100] direction. The examined surfaces were all platinum-coated by a Hummer 6.2 sputtering system (Anatech, Union City, CA). Film thickness was measured at multiple locations and then averaged over at least five measurements. The thickness of the films was measured on the specimen's central, horizontal cross-sectional surface, so that valid comparisons can be made to probe the growth kinetics of the sol–gel layers and the multilayer films. The error bars of thickness in all figures represent ± 1.0 standard deviation of these multiple measurements. The specimens were also characterized by X-ray diffraction (XRD), using a Scintag XDS 2000 diffractometer (Cupertino, CA) with Cu-Kα radiation ($\lambda = 1.5418$ Å) and Fourier transform infrared spectroscopy (FTIR, using a Thermo-Nicolet Magna 550 spectrometer, Madison, WI). The absorbance infrared spectra were obtained from 400 to 4000 cm^{-1} with a resolution of 2 cm^{-1}.

The hardness and elastic modulus of the specimens were determined by nanoindentation experiments using an MTS Nano Indenter XP (MTS Nano Instruments, Inc., Oak Ridge, Tennessee), under both the regular and dynamic contact module (DCM) modes. All indentation tests followed the ISO 14577 method (ISO, 2002) under the load control mode and used diamond Berkovich indenter tips. The well recognized Oliver and Pharr[58,59] method was used to derive the hardness and Young's modulus from each indentation. To eliminate the effect of substrate, multiple indentations were made on each sample with varied maximum indentation loads. The Tuck *et al.*[60] and Wei *et al.*[61] methods were adopted to extract the true hardness and elastic modulus of the thin films, respectively. Further details on the nanoindentation testing can be found in Wei *et al.*[61]

3. Results and discussion

3.1. Overview of multilayer characteristics and linear LbL growth

The characteristics of the $\{MMT_x\text{-(sol–gel } ZrO_2)\}_n$ multilayers with different deposition cycles were presented first. Fig. 1(a) shows that a linear relationship exists between the film thickness and the number of deposition cycles for the multilayers prepared under a set of selected control parameters. After 30 deposition cycles, the thickness reaches ~1950 nm; yet the layered structure and linear relationship are well maintained (Fig. 1). Under this particular synthesis condition (*i.e.*, 10 min holding in a 0.15 M precursor solution, and other parameters specified above), the growth rate, defined as the thickness increment per deposition cycle, is calculated to be ~64 nm per deposition cycle. Representative cross-sectional and in-plane SEM images are shown in Fig. 1(b–g).

The much improved layered and periodic structure, film integrity, and linear growth behavior (as compared with those in our preliminary work[50]) are clearly evident in Fig. 1. These improvements are attributed to the use of better exfoliated MMT suspensions and a set of optimized dipping parameters, as described previously in the "Experimental" section. For example, in one set of the optimization experiments, after the holding time in air was varied from 45 s to 10 min, the thickness of a $\{MMT_x\text{-(sol–gel } ZrO_2)\}_{30}$ multilayer increased only slightly from ~1920 nm to ~1950 nm, and essentially identical layer structure were obtained (images not shown). This demonstrates that a holding time of 45 s in air is long enough to dry the sol–gel ZrO_2 layers before the next dip in the MMT suspension. As such, in this study, all specimens were held in air for a fixed time of 45 s between two consecutive dips. The three parameters, including the precursor concentration, holding time in the precursor solution, and aging time, were varied to probe the growth kinetics of sol–gel layers on MMT surfaces; while others were generally fixed after some extensive optimization experiments.

Given that the dipping direction is vertical, the film thickness of all specimens is uniform along a horizontal cross-section of the substrate, as reflected by the small error bars in all plots. On the other hand, thickness gradients exist along the vertical direction. Such thickness gradients are less than ~10% for specimens that were dipped into the precursor solution for 10 min. However, the thickness gradients along the vertical direction can become significant when the holding time in the precursor is comparable with the total time for both the dipping and withdrawing processes (*i.e.*, ~1 min each for dipping and withdrawing at the current moving speed of 2 cm per minute). This is presumably due to the growth of sol–gel layers during both the dipping and withdrawing processes in the precursor solution, in addition to static holding in the precursor solution. Because the lower part of the substrate has longer time of immersion than the upper part, a thickness gradient develops along the vertical direction. This effect may be beneficially used to make multilayers with controlled gradients of thickness, but this is beyond the scope of this study.

Free-standing films with planar dimensions greater than 0.5 cm were made *via* the sacrificial substrate technique described before. Representative SEM and optical images of a freestanding

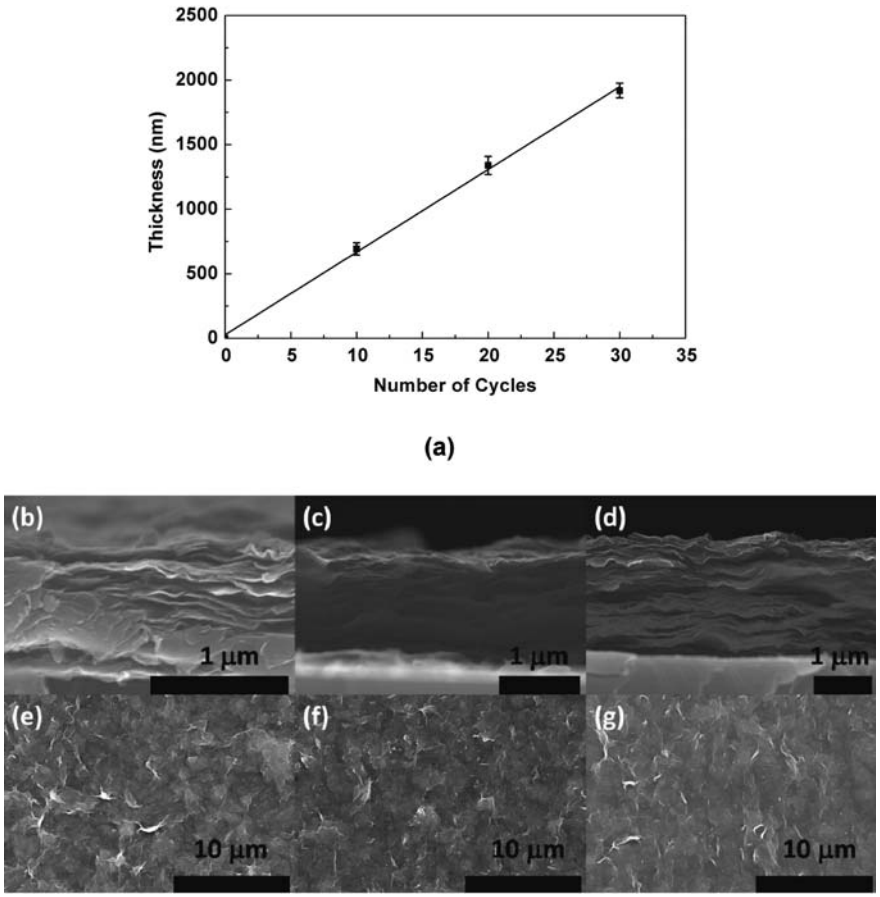

Fig. 1 (a) The relationship between the multilayer thickness and number of deposition cycles for specimens prepared by using 0.15 M precursor solutions, 10 min holding in the precursor, and other fixed parameters specified in the text. Representative cross-sectional and in-plane SEM images of the multilayers prepared by (b, e) 10, (c, f) 20, and (d, g) 30 deposition cycles, respectively.

film are shown in Fig. 2. These images indicate that these multilayers exhibit good structural integrity. Although these multilayers were only air-dried, the interfacial bonding between the MMT and sol–gel ZrO_2 layers is sufficiently strong to permit peeling of the film off the substrate. This proves the feasibility of making larger freestanding multilayers.

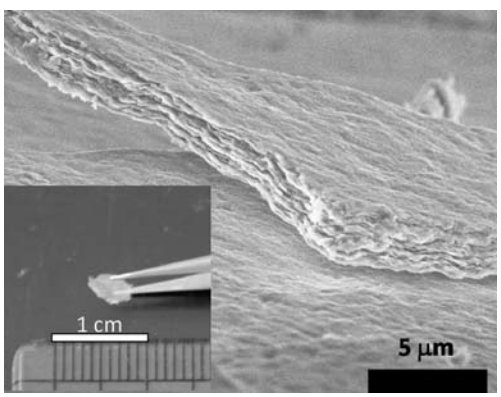

Fig. 2 An SEM image of a piece of free-standing, air-dried $\{MMT_x$-(sol–gel $ZrO_2)\}_{30}$ multilayer. Inset is an optical photograph of a large piece of freestanding multilayer.

3.2. Growth of non-aged sol–gel layers: effect of precursor concentration

In the first set of systematic experiments designed to investigate the mechanism of growing sol–gel ZrO_2 layers on MMT surfaces, $\{MMT_x$-(sol–gel $ZrO_2)\}_{30}$ specimens were synthesized using freshly prepared precursor solutions with varied concentrations of 0.03–0.4 M and three specific holding times (*i.e.*, 0, 45 s, and 10 min). The relationships between the film thickness and precursor concentration are shown in Fig. 3(a). The curve for a holding time of 45 s exhibits a characteristic S-shape. In this curve, the film thickness is almost constant ($\sim$15 nm per deposition cycle) at low precursor solution concentrations ($\leq$0.06 M), but increases rapidly in the middle concentration range of 0.15–0.30 M, and then finally reaches a saturation level of $\sim$70 nm per deposition cycle at high concentrations. The cross-sectional SEM images of selected specimens are shown in Fig. 3(c). Again, the layered structure is clearly observable. With zero holding time in the precursor solution, the film thickness increases only slightly with increasing the precursor concentration, indicating minor and slow deposition of the sol–gel layer during the dipping/withdrawing stage. For a longer holding time of 10 min, the film growth rate (per deposition cycle) approaches the saturation level quickly, and the multilayers are no longer uniform at the

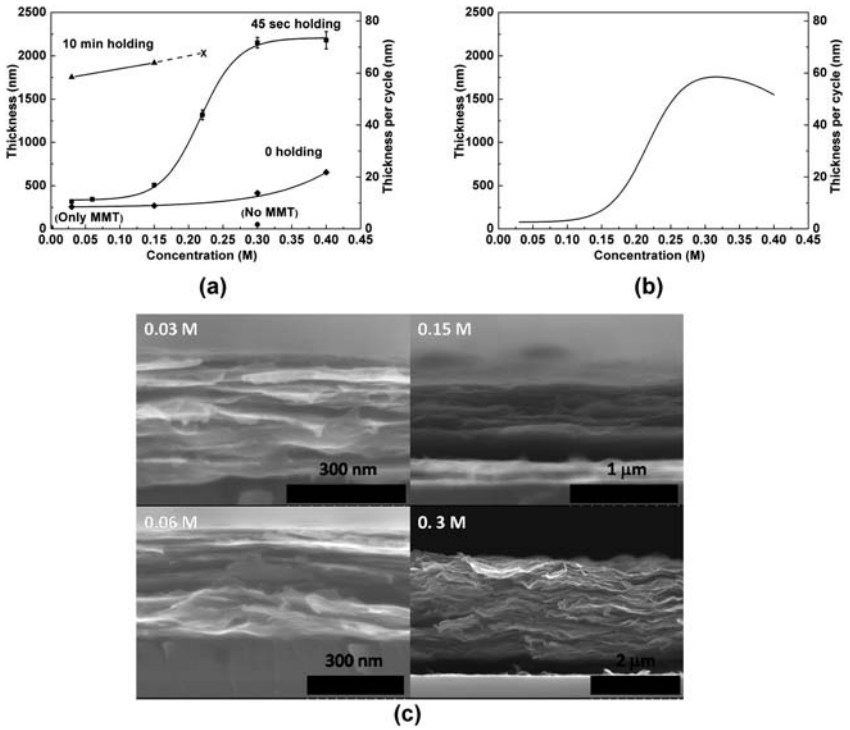

Fig. 3 (a) The relationship between the film thickness and precursor solution concentration. The holding times in the precursor solutions are labeled. The dashed line and the symbol "X" indicate that the films become non-uniform at high concentrations with prolonged holding time due to the gelation of the solution. As a comparison, the two solid cycles represent the measured thickness for films made by dipping only in MMT suspension (labeled as "Only MMT") or only in zirconium acetate hydroxide solution (near the origin point, labeled as "No MMT", holding time = 45 s). (b) The relationship between the estimated net thickness for the sol–gel layers grown during 45 second holdings in precursor solutions and the precursor solution concentration. (c) Representative cross-sectional SEM images. The precursor solution concentrations are labeled; holding time = 45 s. In panels (a) and (b), the double scales of the *y*-axis represent either the total thickness of the multilayer after 30 deposition cycles (left axis) or thickness per deposition cycle (right axis).

high zirconium concentrations (≥0.3 M) due to the gelation of the precursor solution.

In Fig. 3(b), the difference between the film thicknesses obtained by 45 s and 0 holding times is plotted against the precursor solution concentration to estimate the net thickness of the sol–gel ZrO_2 layer that grows during the 45 s static holding in the precursor solution. This curve does not follow the classical mass transfer (diffusion) or interfacial reaction controlled kinetics model, which would both suggest a linear dependence of the sol–gel layer thickness on concentration, using the first order of approximations.[62]

3.3. Growth of non-aged sol–gel layers: effect of holding time

In the second set of systematic experiments designed to investigate the sol–gel layer growth kinetics, the thickness of the multilayers was analyzed as a function of the holding time (0–10 min) in the freshly prepared precursor solutions with two selected concentrations, 0.03 and 0.15 M. The results are shown in Fig. 4(a), while representative cross-sectional SEM images are shown in Fig. 4(c). For both concentrations, the growth of sol–gel layers again exhibits three characteristic regimes: an initial incubation regime with a slow growth speed (to reduce ambiguity, "growth speed" refers to the film thickness change per unit holding time, while "growth rate" is defined as the film thickness change per deposition cycle), an intermediate regime with a high growth speed, and a final saturation regime where the growth speed approaches zero. The maximum growth speeds in the intermediate regime are approximately 20–30 nm per minute of holding time for both curves. The saturation thickness is ~48 nm per deposition cycle for 0.03 M and ~55 nm per cycle for 0.15 M precursor solution. It is interesting to note that the saturation or self-limiting thickness increases only by ~12% when the precursor solution concentration has a fivefold increase from 0.03 to 0.15 M.

With zero holding time in the precursor solution, the multilayer film grows at a rate of ~8 nm per deposition cycle, which is about the same for both concentrations. This net thickness increment per deposition cycle results from the thickness of the MMT layers and the hydrodynamic adsorption of sol–gel ZrO_2 during both the dipping and withdrawing processes. To the first order of approximation, this growth rate can be used as a reference value to estimate the net growth of sol–gel ZrO_2 layers while holding the specimens in the precursor solutions.

To directly analyze the growth kinetics in the 0.03 and 0.15 M solutions, the net thicknesses of the sol–gel ZrO_2 layers, obtained by subtracting the reference value of ~8 nm as discussed above, are re-plotted at a double logarithmic scale in Fig. 4(b). If the growth of a sol–gel ZrO_2 layer on the MMT surfaces were considered as a precipitation (*i.e.*, first-order phase

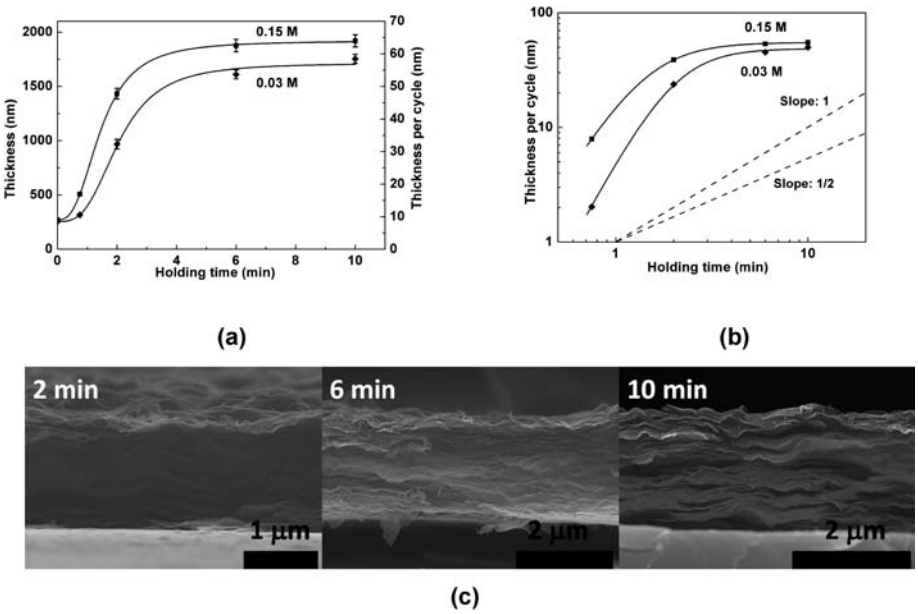

Fig. 4 (a) The multilayer thickness *versus* holding time for two different precursor solution concentrations (0.15 M and 0.03 M). (b) A double logarithmic plot of the estimated net thickness of sol–gel layer grown on the MMT surface per cycle *versus* holding time. (c) Representative cross-sectional SEM images (0.15 M zirconium acetate hydroxide solutions; the holding times are labeled). In panel (a), the double scales of the *y*-axis represent either the total thickness of the multilayer after 30 deposition cycles (left axis) or thickness per deposition cycle (right axis).

transformation) process without electrostatic interactions, the classical kinetic models would be applicable. In such cases, the deposition process would be controlled by either interfacial reaction rates or mass transfer (diffusion) rates.[62] For the former, the sol–gel layer should grow linearly with time (t), *i.e.*, the layer thickness is

$$\chi \propto t \tag{1}$$

For the latter, the sol–gel layer should grow parabolically or the thickness is

$$\chi \propto \sqrt{t} \tag{2}$$

The above two equations can be represented by the two linear lines with slopes of 1 and ½, respectively, in the double logarithmic plot, as indicated by the two dashed lines in Fig. 4(b). However, the experimental data in Fig. 4(b) show that the growth speeds between 0.75 to 2 min exhibit slopes that are greater than those predicted by either interfacial reaction or mass transfer controlled kinetics. It suggests that the sol–gel layer growth in this regime is surface-controlled and is further accelerated by the electrostatic attractions resulting from the large negative surface charges on the MMTs.

Furthermore, at a later stage (*i.e.*, when holding time is greater than 6 min), the further growth of the sol–gel layer virtually stops. In fact, the observed saturation thicknesses in both Fig. 4 and Fig. 3 are in the same range of 50–60 nm per deposition cycle, after subtracting the estimated thickness (*i.e.*, 8 nm per deposition cycle) of MMT layers. This saturation thickness is significantly greater than the commonly known monolayer or submonolayer self-limiting thickness.[63–65] If the growth of sol–gel layer between 0.75 to 2 min holding time is indeed controlled by electrostatic attractions, this observed self-limiting growth of sol–gel layer on the MMT surfaces may be explained, as a hypothesis, by the screening of the electrostatic interactions. To quantify the screening effect and to justify this hypothesis, the Debye length (κ^{-1}) is estimated to be around 30 nm for 0.15 M precursor solution, using the following equation:

$$\kappa^{-1}\ (\text{nm}) = 10/\sqrt{I\ (\text{mM})} \tag{3}$$

where I is the ionic strength, which is estimated to be ~0.1 mM based on the measured pH value of 4.06, assuming that H^+ is the leading cations that are balanced by monovalent anions. Thus, the potential at a distance of 69 nm from the MMT surface drops to 10% of the surface potential. It should be noted that the actual screening effect will change when the sol–gel layer forms on the MMT surface. Because the effective dielectric constant and the charge distribution in the sol–gel layer are both unknown, it is difficult to quantify the screening effect more accurately. Nonetheless, such a simple estimate of the screening length, although not rigorous, supports the above hypothesis.

3.4. Coupling of the growth of MMT and sol–gel ZrO_2 layers

To further examine whether the growth of MMT layers and sol–gel ZrO_2 layers is coupled or independent, two control experiments were conducted to grow MMT only (*i.e.*, by skipping the dips in the precursor solution) and to grow the sol–gel ZrO_2 layer only (*i.e.*, by skipping the dips in the MMT suspension), respectively. When the substrate was dipped in a MMT suspension and deionized water twice for rinsing alternately for 30 deposition cycles, the resultant film's total thickness is less than 20 nm (Fig. 5). Since the thickness of one monolayer of exfoliated MMT (*i.e.*, a 2 : 1 or T–O–T layer in the clay mineralogy concepts) is about 1 nm,[25] the observed overall growth rate of 20 nm (or ~20 MMT T–O–T platelets) in 30 deposition cycles

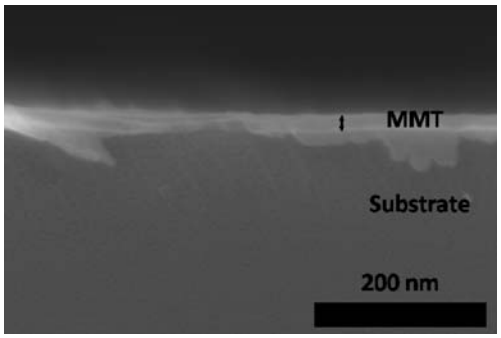

Fig. 5 A representative cross-sectional SEM image for a film made after dipping a substrate in a MMT suspension and rinsing water (twice each cycle) for 30 deposition cycles (*i.e.*, without dipping in a zirconium acetate hydroxide solution).

suggested that the LbL growth is neither linear nor continuous. Instead, after several layers of clay platelets were deposited, further adhesion of clay platelets in subsequent deposition cycles was impeded due to electrostatic repulsions among MMT layers. This observation clearly demonstrates that MMT layers cannot continuously grow without depositing sol–gel ZrO_2 layers in between. For comparison, when the thickness *vs.* concentration curve in Fig. 3(a) for zero time of holding in the precursor solution is extrapolated to 0 M concentration, a growth rate of ~8 nm per cycle (*i.e.*, ~250 nm for 30 deposition cycles) is obtained. This extrapolated growth rate of ~8 nm per deposition cycle is significantly greater than the observed overall growth rate of 20 clay platelets in 30 deposition cycles without depositing sol–gel layers. (It should be noted that the actual thickness of MMT layers per deposition cycle may be slightly lower because this reference level of ~8 nm, which can be obtained *via* extrapolations in either Fig. 3(a) or Fig. 4(a), should still include the thickness of some residual sol–gel oxide films. The XRD results reported in section 3.7 indicated the thickness of MMT stacks is ~2.6 nm, which can be considered as a low-end estimation of the thickness of MMT layers in each deposition cycle.) It is therefore concluded that the MMT deposition mechanisms are remarkably different for the growth with and without the deposition of the sol–gel layers. One possible reason is that the negative surface charges on the MMT will prevent continuous adsorption of additional MMT layers unless a sol–gel oxide was deposited to neutralize or reverse charges on the surface of the growing film.

In the second set of control experiments, substrates were dipped only in the 0.3 M precursor solution and deionized water twice repeatedly, but not in the MMT suspension. It was found that the sol–gel layers grow linearly. The growth rate is estimated to be ~1.6 nm per deposition cycle, as shown in Fig. 6. This value is similar to the size of a zirconia polyoxocation (*i.e.*, ~2 nm[35,66]) that is presumably present in the precursor solutions. This observation suggests that about one monolayer of zirconia polyoxocations was deposited onto the substrate per deposition cycle. This finding is further supported by the fact that, when the holding time increases from 45 s to 10 min, there is virtually no increase in the film thickness (Fig. 6(b) *vs.* (c)). Therefore the growth of sol–gel layers is self-limited to ~1.6 nm per deposition cycle when no MMT layers are involved. All these results suggest that the growth of sol–gel ZrO_2 layers follows a similar

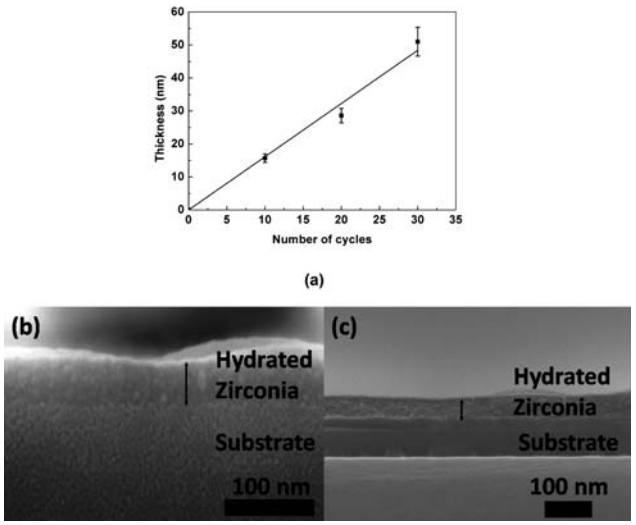

Fig. 6 (a) The thickness of the sol–gel layers *versus* number of deposition cycles (45 s holding in 0.3 M precursor solution; without dipping in a MMT suspension and rinsing). Representative cross-sectional SEM images of films made *via* dipping substrates in 0.3 M zirconium acetate hydroxide solutions for 30 deposition cycles with (b) 45 s and (c) 10 min holding time in the solutions.

mechanism that was proposed to control the successive ionic layer adsorption and reaction (SILAR) process, where an ideal growth of one monolayer of ionic species per deposition cycle is usually expected.[63–65] In contrast, when the sol–gel layers were grown on the MMT surfaces under the same dipping conditions, significantly increased growth rates that are much greater than the monolayer growth were observed. For instance, the total growth rate for a 45 s holding time in a 0.3 M precursor solution is ~70 nm per deposition cycle. As a rough estimate, the growth rate of 8 nm per deposition cycle, obtained by extrapolating the 45 s holding time curve to 0 M precursor solution (Fig. 3(a)), is used to represent the thickness increment of the MMT layers per deposition cycle. The difference of these two values, ~62 nm per deposition cycle, is then attributed to the net growth of the sol–gel layer on the MMT surfaces, which is ~40 times greater than that observed for dipping only in the precursor solution (Fig. 6). This comparison unequivocally shows that the growth rates of sol–gel layers are significantly increased due to the presence of negatively charged MMT layers. This increase can be attributed to primarily the presence of electrostatic attractions, and secondarily the increased surface roughness of the MMT surfaces.

3.5. Additional discussion of possible sol–gel growth mechanisms

To date, the exact sequence for the sol–gel reaction to form ZrO_2 is unknown. A mostly likely process consists of three steps: hydrolysis, which likely results in weakly ionized zirconium polyoxocations of ~2 nm in size;[67] condensation/polymerization, which may generate neutral and soluble zirconium polymer species with a $(Zr^{4+}) : (CH_3COO^-)$ ratio of 1 : 2;[67] and gelation *via* replacing CH_3COO^- groups with OH^- groups on the

polymeric zirconium species, which results in the precipitation of insoluble gels at a $(Zr^{4+}) : (CH_3COO^-)$ ratio of ~1 : 1. Possible surface initiated sol–gel processes for the low and high concentration regions (as shown in Fig. 3(a)) are proposed as follows. At the low concentration region, the precursor solution is likely composed of zirconium polymer species[67] and a smaller portion of zirconium polyoxocations.[68] Since the Na^+ cations on MMT surfaces are exchangeable with other monovalent cations in solution (note that the MMT has an exchange capacity of 92.6 meq per 100 g),[69] Na^+ cations on MMT may exchange with zirconium polyoxocations, leading to the formation of a sub-monolayer of zirconium polyoxocations on MMT surfaces. In the low concentration range (*i.e.*, <~0.1 M) in Fig. 3, the difference in growth rates between 0 and 45 s holding time is small, ~1.4 nm per cycle, which is less than the thickness of one monolayer of zirconium polyoxocations (*i.e.*, 2 nm in size). This suggests that monolayer adsorption *via* cation exchanging may be the main growth process at low concentrations, and additional surface-initiated gelation process is not significant. In the high concentration range (*i.e.*, >~0.2 M) in Fig. 3(a), the growth rate difference is more significant. This indicates that surface-initiated gelation may be dominant, and electrostatic interactions can enhance the deposition of sol–gel layer. This surface initiated sol–gel process may be sustained by the precipitation *via* replacing the CH_3COO^- groups with OH^- groups on polymeric zirconium species.

3.6. Effects of aging

With no aging, the viscosity of the freshly prepared zirconium acetate hydroxide solution is small or not measurable by a commercial viscosity meter. Thus, the deposition of sol–gel ZrO_2 layers is likely a surface sol–gel process (in other words, no significant gelation in the bulk solution). When the precursor solution is aged, a sol–gel process will occur in the bulk solution, resulting in a significant increase in viscosity.[70] To investigate how such an aging process affects sol–gel layer deposition and growth, a 0.15 M precursor solution was first aged for various durations at 60 °C before it was used to prepare the $\{$MMT-(sol–gel $ZrO_2)\}_{30}$ multilayers. It was found that the 0.15 M precursor solution turned into a viscous gel after aging for 21 h at 60 °C. At such viscosity, uniform multilayer films could no longer be synthesized. As such, in this series of experiments, the maximum aging time was limited to 14 h.

Fig. 7 shows the relationships between the multilayer thickness and aging time for two sets of specimens that were prepared with 0 and 45 s holding time in aged precursor solutions. In general, the aging process causes an increase in the viscosity of the sol and affects the hydrodynamics of the film growth during the withdrawing step and, presumably to a lesser extent, advancing/dipping step. Empirically, it is common to assume that the viscosity (η) of an aged sol increases exponentially with aging time (t), *i.e.*, $\eta = A_\eta e^{t/\tau}$, where A_η and τ are two constants.[70] Then, the entrained film thickness (h, which scales the final total film thickness) during dipping can be estimated by the Landau–Levich equation:[71]

$$h = 0.94(A_\eta e^{t/\tau} U)^{2/3}/\gamma_{LV}^{1/6}(\rho g)^{1/2} \quad (4)$$

where U is the withdrawal speed and ρ is the density of the sol. We may assume, for simplicity, that the surface tension (γ_{LV}) is a constant,[72] and there is no volume change during gelation. Then, eqn (4) can be simplified as

$$h \propto e^{\frac{2}{3\tau}t} \quad (5)$$

In other words, the thickness of the sol–gel film deposited during the hydrodynamic process is an exponential function of aging time, at a first order of approximation. To compare the above equation with experimental data, the net thickness of the sol–gel ZrO_2 layers is estimated in the hydrodynamic process *via* subtracting the thickness of MMT layers of ~8 nm per deposition cycle (which was estimated by extrapolating to 0 precursor solution concentration in Fig. 3(a) from the actual measured multilayer thickness; see the discussion above). This corrected curve, shown as Curve III in Fig. 7(a), can be well fitted by an exponential function [$h = 60.1 \times \exp(t\ (\text{hours})/14.9) - 58.7\ (\text{nm/cycle})$]. Hence, this agreement supports that the deposition of aged sol is controlled by a hydrodynamic process following the Landau–Levich equation. The aging time constant can be intentionally tuned by changing precursor concentration, solution pH, temperature, and other parameters that affect the sol–gel kinetics. It should be noted that the Landau–Levich equation is not applicable when the aging time, t, approaches zero, where the film growth is no longer controlled by hydrodynamics. This may explain the occurrence of an extra constant in the fitted thickness *vs.* aging time function. Another interesting finding is that the difference between the thicknesses of multilayers for the two sets of specimens is almost independent of the aging time, as shown in Curves I *vs.* II in Fig. 7(a). This again indicates that the sol–gel layer growth is controlled by hydrodynamics (*i.e.*, the increase in viscosity does not significantly affect the deposition of sol–gel layers during the holding in the aged sols). Representative cross-sectional SEM images of multilayers made using aged precursors are shown in Fig. 7(b); these images show that nanoscale layered structures are well maintained in these multilayers, where the growth of sol–gel layers is controlled by hydrodynamics.

3.7. Structure and effects of annealing

The as-deposited films are typically hydrated and contain some residual acetate groups, which can be removed by controlled annealing. Thus, we conducted further experiments to investigate the thermal stability and the changes in molecular structures of the $\{MMT_x$-(sol–gel $ZrO_2)\}_{30}$ multilayer after annealing at different temperatures. FTIR spectra of an as-deposited specimen and the specimens annealed between 200 and 600 °C (for 2 h) are shown in Fig. 8(a). The characteristic vibration bands of MMT and zirconium acetate are present in an as-deposited multilayer specimen. The 3625 cm^{-1} band is related to the stretching mode of O–H attached to the Al or Mg in the MMT octahedral sheet layer.[69] The 1121 and 1050 cm^{-1} bands are related to the two Si–O stretching bands for apical and basal oxygen in the MMT, respectively. The 523 cm^{-1} band is related to Si–O–Al bending in the MMT.[73] On the other hand, the two major bands of zirconium acetate can be found at 1568 and 1448 cm^{-1}, which are related to asymmetric and symmetric COO stretching bands.[74] The 646 cm^{-1} band is related to Zr–O

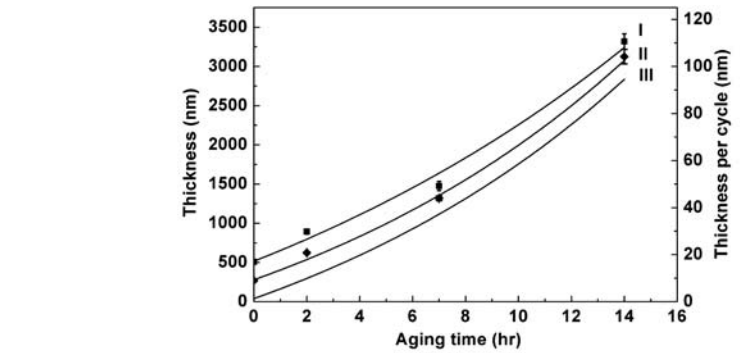

(a)

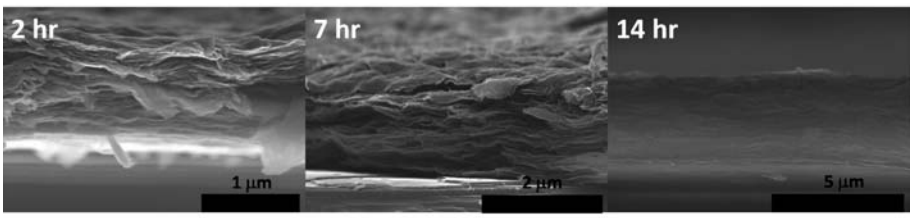

(b)

Fig. 7 (a) The multilayer thickness *versus* precursor solution aging time at 60 °C for holding times of 45 (Curve I) and 0 s (Curve II). Curve III represents the net thickness of hydrodynamic deposited sol–gel layers (estimated by subtracting the thickness of MMT layer from Curve II). (b) Representative cross-sectional SEM images of selected multilayers corresponding to Curve I.

stretching band.[75] The 465 cm^{-1} band may be related to Zr–O bending from tetragonal Zr–O.[76,77] These bands indicate that hydrated sol–gel ZrO_2 and some residual acetate groups are present in the as-deposited films.

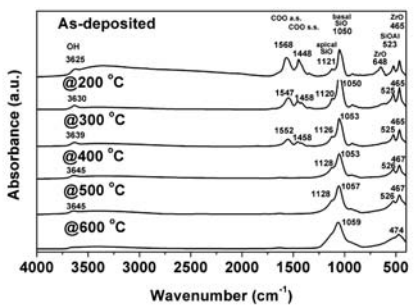

(a)

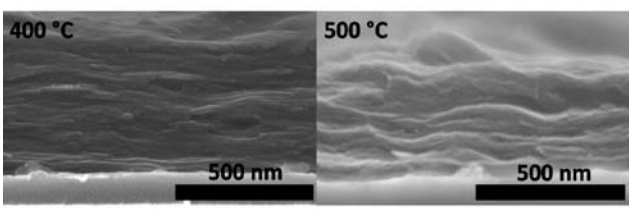

(b)

Fig. 8 (a) FTIR spectra of an as-deposited $\{MMT_x\text{-(sol–gel } ZrO_2)\}_{30}$ multilayer and multilayers annealed at different temperatures. All specimens were made using 0.15 M precursor solution and a holding time of 45 s. (b) Cross-sectional SEM images of selected annealed multilayers.

When the multilayers were annealed, the molecular structure changed gradually (Fig. 8 (a)). Two strong COO stretching bands weaken with increasing annealing temperature and eventually disappear at 400 °C. The 646 cm^{-1} band from the Zr–O stretching band disappears at 300 °C, inferring the complete removal of CH_3COO groups at 300 °C. The 1121 cm^{-1} band of Si–O (apical oxygen) stretching becomes a weak shoulder at 500 °C and virtually disappears at 600 °C, indicating the onset of the MMT crystal structure collapse at this temperature. The disappearance of 3625 cm^{-1} OH stretching at 600 °C is further evidence for the disintegration of MMT crystal structure. However, the 465 cm^{-1} band, which is the combination of Si–O and Zr–O bending bands, remained strong at all temperatures but shifted slightly to 474 cm^{-1} at 600 °C. In summary, annealing at ~400 °C results in the formation of MMT-zirconia multilayers with MMT crystal structures intact, but the acetate residues and moisture are removed. Selected SEM images of annealed multilayers are shown in Fig. 8(b), and these images show that the layered structures are well maintained after annealing at 400–500 °C.

The averaged thickness of an as-deposited (air-dried) $\{MMT_x\text{-(sol–gel } ZrO_2)\}_{30}$ multilayer is 507 nm ± 11 nm. After annealing at 400 °C for 2 h, the average thickness is reduced by ~13% to 439 nm ± 15 nm. It is further reduced to 381 nm ± 8 nm after annealing at 600 °C for 2 h (*i.e.*, ~25% linear shrinkage from the as-deposited multilayer).

The XRD patterns of as-deposited and annealed $\{MMT_x\text{-(sol–gel } ZrO_2)\}_{30}$ multilayers are shown in Fig. 9. A strong MMT (001) peak with a *d*-spacing of ~1.2 nm was found in the XRD pattern of as-deposited multilayer, implying the presence of stacked nanoclay platelets, which are likely orientated parallel to

the surface. The nominal crystallite size (perpendicular to the MMT (001) plane) calculated based on the Scherrer equation was ~2.6 nm. It should be noted that the actual crystallite size can be greater than that estimated from the Scherrer Equation, because the variation in the interlayer spacing (possibly due to water adsorption and partial cation exchanges) and stacking disorder among particles may also result in broadening of this XRD peak. Consistently, our kinetic growth study discussed above suggested that <~8 nm thick MMTs were deposited in each deposition cycle (see elaboration in section 3.4). After annealing at 400 °C, the MMT (001) peak became weaker, but it is still distinguishable. This indicated the partial loss of crystallinity of the MMT stacks. When the annealing temperature was increased to 600 °C, the MMT (001) peak virtually disappeared, indicating the disintegration of MMT stacks. These XRD results of annealing effects are consistent with the FTIR results discussed above. After annealing at 400–600 °C, a wide bump appeared at ~2θ = 29–30°, indicating the partial crystallization of ZrO_2. This board zirconia peak appears to be the sum of a diffused monoclinic ZrO_2 $(-111)_m$ peak ($2\theta = 27.3°$) and a diffused tetragonal ZrO_2 $(111)_t$ peak ($2\theta = 30.3°$), as labeled in Fig. 9. The equivalent crystallite size calculated based on the Scherrer equation was ~1.5–2.2 nm (dependent on whether we consider this bump as a single peak or double peaks), indicating that ZrO_2 is poorly crystallized (largely amorphous or possibly nanocrystalline) after annealing at 400–600 °C.

3.8. Mechanical properties

Table 1 summarizes the derived mechanical properties of several multilayer films. In general, both the hardness H and elastic modulus E of the as-deposited films are much lower than those of the annealed ones, because the former contains a significant amount of water in the structure, present either as absorbed water inside the MMT interlayer spaces or as hydrated water in the hydrated oxide gels. Annealing significantly enhances the hardness and elastic modulus. As the data analysis has eliminated the substrate effect, the effect of film thickness on the hardness and mechanical properties is also removed. Consistently, measurements of the two films, $\{MMT_x\text{-(sol–gel } ZrO_2)\}_{30}$ and $\{MMT_x\text{-(sol–gel } ZrO_2)\}_{60}$, resulted in similar results. Furthermore, the inclusion of a soft oxide, SnO_2, significantly reduces both the hardness and elastic modulus of a $\{MMT_x\text{-(sol–gel } ZrO_2)\text{-}MMT_x\text{-(sol–gel } SnO_2)\}_{15}$ multilayer. This particular result clearly demonstrated that the properties (*e.g.*, elastic modulus) of these nanocomposite multilayers can be intentionally tuned *via* changing their designed structure. Finally, the measured elastic modulus of the $\{MMT_x\text{-(sol–gel } ZrO_2)\}_n$ multilayers are ~40–45 GPa, which are significantly lower than those of monoclinic ZrO_2 (~244 GPa at room temperature[78–80]) and MMT (250–260 GPa for a single MMT nanoplatelet[81]). Since it is well established that the elastic modulus of a ceramic material depends on its porosity (*e.g.*, a prior study showed that the modulus of monoclinic ZrO_2 decreases from >200 GPa to ~92 GPa with 22.8% porosity[79]), this result suggested the presence of significant porosity in these nanocomposite multilayers even after annealing.

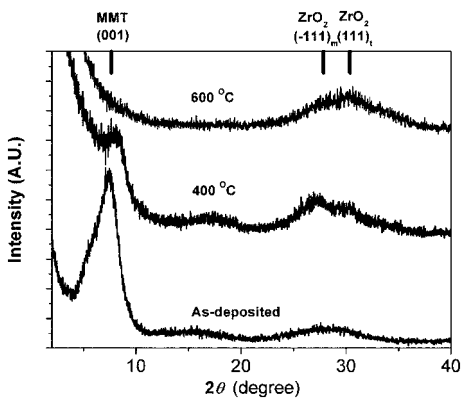

Fig. 9 XRD patterns of as-deposited and annealed $\{MMT_x\text{-(sol–gel } ZrO_2)\}_{30}$ multilayers. Annealing temperatures are indicated.

3.9. Other sol–gel oxide "glued" multilayers and potential applications

The $\{MMT_x\text{-(sol–gel } ZrO_2)\}_n$ multilayers were synthesized for the first time in our studies. It is particularly worth emphasizing that the LbL assembly of such multilayers using sol–gel oxides, instead of polymers or polyelectrolytes, as structural "glues" is a new concept. To demonstrate that this methodology can be extended to other metal oxides, a $\{MMT_x\text{-(sol–gel } SnO_2)\}_{30}$ multilayer was synthesized. A representative cross-sectional SEM image is shown in Fig. 10.

Because of their all-inorganic building units and distinct structure, these new multilayers are expected to have applications such as high-temperature gas membranes, sensors, and microelectromechanical system (MEMS) structure components, among others. Although future studies are needed to explore and verify these applications, a few example potential applications are discussed below. First, the application of such multilayers as a class of novel high-temperature filtering membranes with tortuous paths can be envisioned. In general, the inorganic membranes possess high thermal stability, chemical stability in

Table 1 The measured hardness and elastic modulus of clay-oxide multilayers prepared using 0.40 wt.% clay concentration

Specimen		Hardness H (GPa)	Modulus E (GPa)
$\{MMT_x\text{-(sol–gel } ZrO_2)\}_{30}$	As-deposited	0.33	9.94
	Annealed at 600 °C	1.68	43.75
$\{MMT_x\text{-(sol–gel } ZrO_2)\}_{60}$	As-deposited	0.39	9.36
	Annealed at 600 °C	1.86	40.69
$\{MMT_x\text{-(sol–gel } ZrO_2)\text{-}MMT_x\text{-(sol–gel } SnO_2)\}_{15}$	As-deposited	0.43	6.20
	Annealed at 400 °C	1.32	19.4
	Annealed at 600 °C	1.50	30.72

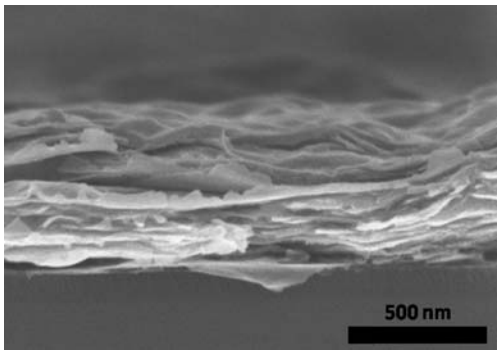

Fig. 10 A representative cross-sectional SEM image of an as-deposited $\{MMT_x\text{-(sol–gel } SnO_2)\}_{30}$ film, indicating that this new methodology can be extended to other metal oxides.

a wide pH range, structural integrity, mechanical strength and stiffness, and long-term durability.[82] More specifically, it is well known that zirconia[83] or zirconia composites[84–87] made by sol–gel processes are good membrane materials bearing nanometer-sized pores. These membranes can be used for high-temperature CO_2 separation,[88] hydrogen production, and purification.[82] In $\{MMT\text{-(sol–gel } ZrO_2)\}_n$ multilayers, the distinct layered structure and the inclusion of the clay nanoplatelets or other nanosheets as tiny barriers in the structure lead to the formation of tortuous paths throughout the film. Second, freestanding MMT-zirconia mutilayers, which have been synthesized in this study (Fig. 2), can be used in micro-cantilevers based on these sensors. Other similar ultrathin cantilever sensors have already been developed by using polymer-ceramic nanocomposites synthesized by LbL assembly.[49] However, cantilever sensors made of all inorganic nanoclay-oxide multilayers are more suitable for high-temperature applications. Third, "photonic clays" or one-dimensional photonic crystals made of spin-coated clay-TiO_2 multilayers have recently been developed as a new type of clay-based chemical sensor.[89,90] Substituting the spin-coated clay layers in the "photonic clays" with the $\{MMT_x\text{-(sol–gel oxide)}\}_n$ multilayers can in principle lead to a better control of thickness, composition, periodicity, and nanoporosity to separate the effects of adsorption, ion exchange, and intercalation for a better selectivity of sensing. Finally, the LbL assembly technique, developed in this study for the use of sol–gel oxides as structural "glues", can be further adapted to synthesize more complex multilayers *via* incorporating other structural and functional materials or components. Further integration of various active (*e.g.*, piezoelectric or magnetic) oxide and non-oxide ceramic materials may enable a versatile yet inexpensive approach to fabricate actuators and sensors. Moreover, other types of nanosheets (*e.g.*, exfoliated layered double hydroxides, MoS_2, or graphenes) can be used to replace nanoclays. Future studies are needed in this direction to demonstrate the feasibility and applications of these more exotic sol–gel oxide based multilayers.

In summary, the success of replacing polyelectrolytes by sol–gel oxides as structural "glues" in LbL assembly of multilayers suggests that opportunities exist for the fabrication of a wide range of new nanostructured multilayers for specifically tailored applications.

4. Conclusions

We report an optimized LbL synthesis route to fabricate a new class of multilayers, $\{MMT_x\text{-(sol–gel } ZrO_2)\}_n$ with an ordered layer structure and sol–gel oxide layers as structural "glues". The film growth rate can be controlled between ~10 nm and ~60 nm per cycle *via* varying the precursor concentration, holding time in the precursor solution, and precursor aging time. A series of systematic experiments and kinetic studies led to the following main conclusions. First, the growth of the MMT and sol–gel ZrO_2 layers is strongly coupled, and these two oppositely charged building units can enhance each other significantly, primarily due to electrostatic attractions. Second, the growth kinetics of the sol–gel layers cannot be explained by simple mass diffusion or interfacial reaction controlled kinetic models, indicating that the electrostatic interactions may significantly impact the growth of sol–gel ZrO_2 layers on the MMT surfaces. Third, the growth of sol–gel ZrO_2 layers on MMT surfaces exhibit a self-limiting thickness of ~50–60 nm, which may be explained by the screening of the electrostatic interactions. Fourth, when the zirconium acetate hydroxide solutions are aged, the growth of sol–gel layers is controlled by a hydrodynamic process that obeys the well-known Landau–Levich model. Fifth, isothermal annealing at ~400 °C will dehydrate the multilayers and remove the residue acetate groups without damaging the MMT nanoplatelets and the ordered layer structure of the films. Sixth, the mechanical properties (hardness and elastic modulus) of these composite multilayers have been measured. Nanomechanical measurements also showed that the elastic modulus (and presumably other properties) of these composite multilayers can be intentionally tuned by changing the multilayer design and that significant porosity is present in these multilayers even after annealing. Finally, we demonstrated that this newly developed methodology can be extended to other metal oxides by synthesizing a $\{MMT_x\text{-(sol–gel } ZrO_2)\}_n$ multilayer.

This study demonstrated the feasibility of replacing polyelectrolytes by sol–gel oxides as "glues" to fabricate LbL assembled multilayers. Various potential applications for this new class of all-inorganic $\{MMT_x\text{-(sol–gel } ZrO_2)\}_n$ multilayers, as well as other types of $\{nanosheet_x\text{-(sol–gel oxide)}\}_n$ multilayers with similar structures, can be envisioned.

Acknowledgements

This work is supported by a National Science Foundation CAREER award (Grant No. DMR-0448879). The authors thank Dr J. Hudson and D. Cash for assistance in using SEM, and K. Ivey for assistance in FTIR measurement. K. M. Cooke was supported by the EUREKA! Program, which allows Clemson University incoming freshmen, in the Calhoun Honors College, to conduct five-week summer research prior to their undergraduate study. Constructive and helpful comments from three anonymous reviewers are also gratefully acknowledged.

References

1 J. H. Fendler, *Chem. Mater.*, 1996, **8**, 1616.
2 J. L. Lutkenhaus and P. T. Hammond, *Soft Matter*, 2007, **3**, 804.
3 P. T. Hammond, *Adv. Mater.*, 2004, **16**, 1271.

4 P. Bertrand, A. Jonas, A. Laschewsky and R. Legras, *Macromol. Rapid Commun.*, 2000, **21**, 319.
5 R. H. A. Ras, Y. Umemura, C. T. Johnston, A. Yamagishi and R. A. Schoonheydt, *Phys. Chem. Chem. Phys.*, 2007, **9**, 918.
6 K. Ariga, J. P. Hill and Q. M. Ji, *Phys. Chem. Chem. Phys.*, 2007, **9**, 2319.
7 S. P. Jiang, Z. C. Liu and Z. Q. Tian, *Adv. Mater.*, 2006, **18**, 1068.
8 Z. Y. Tang, Y. Wang, P. Podsiadlo and N. A. Kotov, *Adv. Mater.*, 2006, **18**, 3203.
9 Y. Wang, A. S. Angelatos and F. Caruso, *Chem. Mater.*, 2008, **20**, 848.
10 G. Decher, *Science*, 1997, **277**, 1232.
11 G. Decher, M. Eckle, J. Schmitt and B. Struth, *Curr. Opin. Colloid. Interf. Sci.*, 1998, **3**, 32.
12 D. W. Kim, A. Blumstein, J. Kumar and S. K. Tripathy, *Chem. Mater.*, 2001, **13**, 2742.
13 P. Podsiadlo, Z. Q. Liu, D. Paterson, P. B. Messersmith and N. A. Kotov, *Adv. Mater.*, 2007, **19**, 949.
14 J. F. Quinn, A. P. R. Johnston, G. K. Such, A. N. Zelikin and F. Caruso, *Chem. Soc. Rev.*, 2007, **36**, 707.
15 E. R. Kleinfeld and G. S. Ferguson, *Science*, 1994, **265**, 370.
16 D. B. Mitzi, *Chem. Mater.*, 2001, **13**, 3283.
17 N. A. Kotov, S. Magonov and E. Tropsha, *Chem. Mater.*, 1998, **10**, 886.
18 P. Podsiadlo, S. Paternel, J. M. Rouillard, Z. F. Zhang, J. Lee, J. W. Lee, L. Gulari and N. A. Kotov, *Langmuir*, 2005, **21**, 11915.
19 G. S. Ferguson and E. R. Kleinfeld, *Adv. Mater.*, 1995, **7**, 414.
20 Y. Lvov, K. Ariga, I. Ichinose and T. Kunitake, *Langmuir*, 1996, **12**, 3038.
21 Z. Tang, N. A. Kotov, S. Magonov and B. Ozturk, *Nat. Mater.*, 2003, **2**, 413.
22 N. A. Kotov, T. Haraszti, L. Turi, G. Zavala, R. E. Geer, I. Dekany and J. H. Fendler, *J. Am. Chem. Soc.*, 1997, **119**, 6821.
23 P. Podsiadlo, A. K. Kaushik, E. M. Arruda, A. M. Waas, B. S. Shim, J. Xu, H. Nandivada, B. G. Pumplin, J. Lahann, A. Ramamoorthy and N. A. Kotov, *Science*, 2007, **318**, 80.
24 H. van Olphen, in *An Introduction to Clay Colloid Chemistry*, John Wiley & Sons, Hoboken, NJ, 1963, pp. 64.
25 S. M. Auerbach, K. A. Carrado, P. K. Dutta, *Handbook of Layered Materials*, CRC Press, Boca Raton, FL, 2004.
26 E. Munch, M. E. Launey, D. H. Alsem, E. Saiz, A. P. Tomsia and R. O. Ritchie, *Science*, 2008, **322**, 1516.
27 R. V. Bellamkonda, *Nat. Mater.*, 2008, **7**, 347.
28 K. Tamura, S. Yokoyama, C. S. Pascua and H. Yamada, *Chem. Mater.*, 2008, **20**, 2242.
29 C. Ortiz and M. C. Boyce, *Science*, 2008, **319**, 1053.
30 L. J. Bonderer, A. R. Studart and L. J. Gauckler, *Science*, 2008, **319**, 1069.
31 H. D. Wagner, *Nat. Nanotechnol.*, 2007, **2**, 742.
32 J. Edwards, *Chem. World*, 2007, **4**, 31.
33 C. Jiang and V. V. Tsukruk, *Adv. Mater.*, 2006, **18**, 829.
34 G. Gao, H.-G. Hong and T. E. Mallouk, *Acc. Chem. Res.*, 1992, **25**, 420.
35 J. W. Johnson, J. F. Brody, R. M. Alexander, L. N. Yacullo and C. F. Klein, *Chem. Mater.*, 1993, **5**, 36.
36 J.-M. Yeh and K.-C. Chang, *J. Ind. Eng. Chem.*, 2008, **14**, 275.
37 R. K. Iler, *J. Colloid Interface Sci.*, 1966, **21**, 569.
38 D. Lee, M. F. Rubner and R. E. Cohen, *Nano Lett.*, 2006, **6**, 2305.
39 D. Lee, D. Omolade, R. E. Cohen and M. F. Rubner, *Chem. Mater.*, 2007, **19**, 1427.
40 D. Lee, Z. Gemici, M. F. Rubner and R. E. Cohen, *Langmuir*, 2007, **23**, 8833.
41 X. Zhang, Y. Wang, X. Chen and W. Yang, *Mater. Lett.*, 2008, **62**, 1613.
42 S. W. Lee, B.-S. Kim, S. Chen, Y. Shao-Horn and P. T. Hammond, *J. Am. Chem. Soc.*, 2009, **131**, 671.
43 J. Kim, S. W. Lee, P. T. Hammond and Y. Shao-Horn, *Chem. Mater.*, 2009, **21**, 2993.
44 A. Kumar, A. B. Mandale and M. Sastry, *Langmuir*, 2000, **16**, 6921.
45 M. D. Musick, C. D. keating, L. A. Lyon, S. L. Botsko, D. J. Pena, W. D. Holliway, T. M. McEvoy, J. N. Richardson and M. J. Natan, *Chem. Mater.*, 2000, **12**, 2869.
46 Z.-S. Wang, T. Sasaki, M. Muramatsu, Y. Ebina, T. Tanaka, L. Wang and M. Watanabe, *Chem. Mater.*, 2003, **15**, 807.
47 Y. Zhou, R. Ma, Y. Ebina, K. Takada and T. Sasaki, *Chem. Mater.*, 2006, **18**, 1235.
48 A. A. Mamedov and N. A. Kotov, *Langmuir*, 2000, **16**, 5530.
49 F. Hua, T. Cui and Y. M. Lvov, *Nano Lett.*, 2004, **4**, 823.
50 H. Chen, G. Zhang, K. Richardson and J. Luo, *J. Nanomaterials*, 2008, **2008**, 749508.
51 P. K. Arcot and J. Luo, *Mater. Lett.*, 2008, **62**, 117.
52 P. K. Arcot and J. Luo, *Surf. Coat. Technol.*, 2008, **202**, 2690.
53 J. Jeon, V. Panchagnula, J. Pan and A. V. Dobrynin, *Langmuir*, 2006, **22**, 4629.
54 J. W. Ostrander, A. A. Mamedov and N. A. Kotov, *J. Am. Chem. Soc.*, 2001, **123**, 1101.
55 N. A. Kotov, T. Haraszti, L. Turi, G. Zavala, R. E. Geer, I. Dekany and J. H. Fendler, *J. Am. Chem. Soc.*, 1997, **119**, 6821.
56 Y. Lvov, K. Ariga, M. Onda, I. Ichinose and T. Kunitake, *Colloids Surf., A*, 1999, **146**, 337.
57 N. A. Kotov, in *The Fourth International Conference on Nanostructured Materials (NANO '98)*, 1999, vol. 12, pp. 789–796.
58 W. C. Oliver and G. M. Pharr, *J. Mater. Res.*, 2004, **19**, 3.
59 W. C. Oliver and G. M. Pharr, *J. Mater. Res.*, 1992, **7**, 1564.
60 J. R. Tuck, A. M. Korsunsky, D. G. Bhat and S. J. Bull, *Surf. Coat. Technol.*, 2001, **139**, 63.
61 Z. Wei, G. Zhang, H. Chen, J. Luo, R. Liu and S. Guo, *J. Mater. Res.*, 2009, **24**, 777.
62 R. W. Balluffi, S. M. Allen, W. C. Carter, R. A. Kemper, *Kinetics of Materials*, John Wiley and Sons, Hoboken, NJ, 2005, pp. 645.
63 Y. F. Nicolau, *Appl. Surf. Sci.*, 1985, **22–23**, 1061.
64 T. P. Niesen and M. E. D. Guire, *J. Electroceram.*, 2001, **6**, 169.
65 T. P. Niesen and M. E. D. Guire, *Solid State Ionics*, 2002, **151**, 61.
66 L. M. Gandia, R. Toranzo, M. A. Vicente and A. Gil, *Appl. Catal., A*, 1999, **183**, 23.
67 A. Pizzi, K. L. Mittal, *Handbook of Adhesive Technology*, CRC Press, Boca Raton, FL, 2003.
68 J. W. Johnson, J. F. Brody, R. M. Alexander, L. N. Yacullo and C. F. Klein, *Chem. Mater.*, 1993, **5**, 36.
69 R. E. Grim, *Clay Mineralogy*. McGraw-Hill: New York, 1968.
70 C. J. Brinker, G. W. Scherer, *Sol–Gel Science: The Physics and Chemistry of Sol–Gel Processing*, Academic Press, Boston, 1990.
71 C. J. Brinker and A. J. Hurd, *J. Phys.*, 1994, **4**, 1231.
72 C. E. Davis, H. M. Salisbury and M. T. Harvey, *Ind. Eng. Chem.*, 1924, **16**, 161.
73 R. Tettenhorst, *Am. Mineral*, 1962, **47**, 769.
74 A. C. Geiculescu and H. G. Spencer, *J. Sol-Gel Sci. Technol.*, 2000, **17**, 25.
75 G. O. Noonan and J. S. Ledford, *Chem. Mater.*, 1995, **7**, 1117.
76 S. K. Saha and P. Pramanik, *J. Non-Cryst. Solids*, 1993, **159**, 31.
77 F. del Monte, W. Larsen and J. D. Mackenzie, *J. Am. Ceram. Soc.*, 2000, **83**, 628.
78 J. Eichler, U. Eisele and J. Rodel, *J. Am. Ceram. Soc.*, 2004, **87**, 1401.
79 N. N. Ault and H. F. G. Ueltz, *J. Am. Ceram. Soc.*, 1953, **36**, 199.
80 C. F. Smith and W. B. Crandall, *J. Am. Ceram. Soc.*, 1964, **47**, 624.
81 B. Q. Chen and J. R. G. Evans, *Scr. Mater.*, 2006, **54**, 1581–1585.
82 G. Q. Lu, J. C. D. d. Costa, M. Duke, S. Giessler, R. Socolow, R. H. Williams and T. Kreutz, *J. Colloid Interface Sci.*, 2007, **314**, 589.
83 J. C.-S. Wu and L.-C. Cheng, *J. Membr. Sci.*, 2000, **167**, 253.
84 X. Changrong, C. Huaqiang, W. Hong, Y. Pinghua, M. Guangyao and P. Dingkun, *J. Membr. Sci.*, 1999, **162**, 181–188.
85 T. Tsuru, T. Hino, T. Yoshioka and M. Asaeda, *J. Membr. Sci.*, 2001, **186**, 257–265.
86 T. Tsuru, Y. Takata, H. Kondo, F. Hirano, T. Yoshioka and M. Asaeda, *Sep. Purif. Technol.*, 2003, **32**, 23.
87 G. I. Spijksma, C. Huiskes, N. E. benes, H. Kruidhof, D. H. A. Blank, V. G. Kessler and H. J. M. Bouwmeester, *Adv. Mater.*, 2006, **18**, 2165.
88 B. N. Nair, R. P. Burwood, V. J. Goh, K. Nakagawa and T. Yamaguchi, *Prog. Mater. Sci.*, 2009, **54**, 511.
89 B. V. Lotsch and G. A. Ozin, *Adv. Mater.*, 2008, **20**, 4079.
90 B. V. Lotsch and G. A. Ozin, *ACS Nano*, 2008, **2**, 2065.